https://doi.org/10.5194/egusphere-2026-1311
Preprint. Discussion started: 7 April 2026

Simulating the impacts of utility-scale photovoltaic installations with a physically based coupled WRF-PV model

Yiran Chen[1,2], Jiming Jin[3], Yimin Liu[1,2], Jannik Heusinger[4], Jesús Carrera[5], Zeyu Zhou[3]

[1]State Key Laboratory of Earth System Numerical Modeling and Application, Institute of Atmospheric Physics, Chinese Academy of Sciences, Beijing 100029, China.
[2]College of Earth and Planetary Sciences, University of Chinese Academy of Sciences, Beijing 100049, China.
[3]College of Resources and Environment, Yangtze University, Wuhan 430100, Hubei Province, China.
[4]Institute of Geoecology, Technische Universität Braunschweig, Braunschweig 38106, Germany.
[5]Institute of Environmental Assessment and Water Research (IDAEA), CSIC, Jordi Girona, 18, 08034 Barcelona, Spain.

Correspondence to: Jiming Jin (jiming@188.com), Yimin Liu (lym@lasg.iap.ac.cn)

Abstract. Utility-scale photovoltaic (PV) installations are expanding so significantly that they may alter the surface energy balance and affect the local climate. Yet, simplified or non-coupled PV schemes in regional climate models limit the understanding of the PV climatic impacts. In this study, we developed a physically based, fully coupled WRF-PV model based on the Weather Research and Forecasting (WRF) model. WRF-PV maintains surface energy balance closure between the PV panels and the ground and enables the PV-induced radiative and thermal effects to feed back to the atmosphere dynamically. We used this model to perform two regional simulations, WRF_PV (with PV panels) and WRF_CTL (without PV panels), in northwestern China, a major PV deployment region. Our results indicated that WRF_PV captured observed spatial and diurnal climate features, and improved the simulation of skin temperature relative to WRF_CTL. PV installations reduced daytime skin temperature by 0.9 °C but warmed near-surface air by 1.8 °C in summer. Additionally, PV-induced enhanced sensible heating, weakened lower-atmospheric stability, and promoted low-level cloud formation, causing a reduction in downward shortwave radiation by about 1%. Moreover, precipitation shifted toward extremes, accompanied by minor reductions in moderate rainfall. This study shows that modeling PV-land surface processes is needed for regional climate models to adequately assess the impacts of utility-scale PV installation.

1 Introduction

Solar energy has grown rapidly worldwide, motivated by the urgent need to abate greenhouse gas emissions and promote the sustainable energy transition (Haegel et al., 2019). Photovoltaic (PV) power, in particular, has expanded rapidly, and utility-scale PV farms have become a major contributor to new renewable energy capacity (IRENA, 2019). By 2022, the global cumulative PV capacity had reached 1,064 GW, with China alone accounting for 393 GW, corresponding to more than 3,000 km^2 of installed PV area (IRENA, 2023; Lyu et al., 2024a), 4.5 times the area within the Fifth Ring Road of Beijing. A considerable portion of these installations is located in semi-arid and arid regions where abundant solar resources

https://doi.org/10.5194/egusphere-2026-1311
Preprint. Discussion started: 7 April 2026

and land availability support utility-scale PV facilities (Lyu et al., 2024b). The rapid expansion of utility-scale PV installations raises concerns about potential environmental impacts.

PV installations replace natural land cover with panel arrays and modify surface physical characteristics. Utility-scale PV installations over barren land reduce surface albedo, leading to greater shortwave absorption and higher daytime net radiation (Li et al., 2022; Ying et al., 2023). In addition, the shading effect of the PV panels reduces the downward shortwave radiation reaching the ground (Armstrong et al., 2016; Fan and Huang, 2020; Yue et al., 2021; Wei et al., 2024; Zhang et al., 2024). Furthermore, PV panels have a lower heat capacity than natural surfaces, causing rapid thermal responses and limited heat storage (Hasan et al., 2016). These changes in surface properties suggest that PV installations could influence regional climate conditions, highlighting the importance of assessing these impacts systematically.

Observational studies on the microclimatic effects of utility-scale PV deployment include in situ field measurements and satellite-based remote sensing analyses. Field measurements across multiple PV farms in semi-arid regions revealed consistent yet site-varying microclimatic responses. During daytime, observed skin temperature changes ranged from almost 0 to cooling of 4 °C, while nighttime responses spanned from a slight warming of 0.1 °C to cooling of 2.3 °C (Yang et al., 2017; Chang et al., 2018; Jiang et al., 2021). These skin temperatures were retrieved from emitted longwave radiation, and uncertainties in surface emissivity contributed to the variability in the estimated temperatures. For near-surface air temperature, daytime warming ranged from 0.2 to 2.6 °C, whereas nighttime effects ranged from weak warming of 0.1 to 0.7 °C to cooling of 0.2 to 1.8 °C. (Barron-Gafford et al., 2016; Yang et al., 2017; Broadbent et al., 2019; Wu et al., 2020; Jiang et al., 2021; Li et al., 2023; Zhang et al., 2024). For surface energy fluxes, sensible heat flux increased, with reported daytime enhancements of 25 to 50 W m^{-2} and a daily mean rise of about 18 W m^{-2}, while both latent heat flux and ground heat flux decreased within PV installations (Broadbent et al., 2019; Jiang et al., 2021). Remote sensing analyses similarly reported daytime surface cooling of approximately 0.5 to 2 °C across utility-scale PV farms over broad regions, with nighttime effects generally weaker and ranging from slight cooling to modest warming (Zhang and Xu, 2020; Fan and Huang, 2021; Guoqing et al., 2021; Wang et al., 2024; Xu et al., 2024). These field measurements and remote sensing analyses demonstrated that utility-scale PV installations can systematically alter local energy partitioning and near-surface climate.

These observations highlight the need for physically based PV representations in climate models. Previous studies often simulated PV impacts by prescribing an effective albedo, which was defined as the sum of panel albedo and the percentage of solar radiation converted to electricity. Based on this method, simulations with PV deployed across the Sahara showed global impacts on temperature, precipitation, and cloudiness (Hu et al., 2016; Li et al., 2018; Lu et al., 2021; Long et al., 2024). However, the conclusions depended strongly on the assumed efficiency value, and the energy-balance processes of the panels were not included in their simulations. Several studies incorporated PV effects into the Weather Research and Forecasting (WRF) model through highly parameterized schemes. These schemes modified radiative and heat flux fields to represent the influence of PV installations on the atmosphere (Chang et al., 2020, 2022). Yet, these schemes lacked energy balance closure and physical generality, limiting the understanding of PV climatic impacts. Therefore, a scheme that ensures

https://doi.org/10.5194/egusphere-2026-1311
Preprint. Discussion started: 7 April 2026

energy balance closure and explicitly resolves the energy exchanges among PV panels, the land surface, and the atmosphere is required in climate models.

Heusinger et al. (2020) developed a PV energy balance model, UCRC-Solar, which resolves PV panel surface temperature and the radiative and thermal exchanges of PV panels. The UCRC-Solar was run offline and driven by external meteorological data. The rooftop evaluation further showed that UCRC-Solar captured PV surface temperature and power production in real conditions (Heusinger et al., 2021). Recent studies advanced UCRC-Solar by introducing a PV canopy energy-exchange scheme to better represent turbulent exchange processes in PV arrays (Li et al., 2024). Another study then integrated this scheme into WRF in a one-way coupling framework to simulate the local microclimate effects of PV deployment (Li et al., 2025b). However, the one-way coupling prevents PV-induced radiative and thermal changes from feeding back into the boundary layer. Yin et al. (2025) coupled the UCRC-Solar rooftop PV energy-balance model within the BEP-BEM scheme in WRF and used this system to investigate the impacts of rooftop PV installations on urban microclimate. However, fully coupled implementations of UCRC-Solar have not been extended to quantify the climatic impacts of utility-scale PV farms. Hence, the lack of a fully coupled PV scheme with energy balance closure for utility-scale farms remains a limitation, as PV installations substantially alter radiative forcing, energy partitioning, and local meteorological conditions.

To address these gaps, this study developed a physically based, fully coupled WRF-PV model. This model maintains surface energy closure between PV panels and the ground and allows the thermal and radiative effects to interact dynamically with the atmosphere. The coupled model was applied to a major utility-scale PV deployment area in a semi-arid environment and evaluated against reanalysis data, satellite products, and site observations. By comparing two multi-year simulations with and without PV panels, we quantified the summer climatic impacts of PV deployment. This study provides new insights into these impacts by using a more physically consistent representation than earlier parameterized or offline approaches.

2 WRF-PV model development

2.1 Energy balance of PV panel

The energy balance of PV panels used in this study follows the formulation of Heusinger et al. (2020), and the surface temperature of PV panels (T_{PV}) is governed by the energy balance equation:

$$C_{\mathrm{module}}\frac{dT_{\mathrm{PV}}}{dt} = \mathrm{SW}_{\mathrm{tot}} + \mathrm{LW}^{*}_{\mathrm{PV}} - Q_{H,\mathrm{PV}} - P_{\mathrm{out}}, \quad (1)$$

where C_{module} is the effective heat capacity of the PV panel (J K^{-1} m^{-2}); $\mathrm{SW}_{\mathrm{tot}}$ is the total absorbed shortwave radiation (W m^{-2}); $\mathrm{LW}^{*}_{\mathrm{PV}}$ is the net longwave radiation exchange (W m^{-2}); $Q_{H,\mathrm{PV}}$ represents the sensible heat flux from the panel to the ambient air (W m^{-2}); P_{out} denotes the electrical power output (W m^{-2}).

$\mathrm{SW}_{\mathrm{tot}}$ is calculated as in Heusinger (2021), with the rear-side contribution additionally included (Coimbra, 2025):

https://doi.org/10.5194/egusphere-2026-1311
Preprint. Discussion started: 7 April 2026

$$\mathrm{SW_{tot}} = \left(\mathrm{SW_{dir}} \cdot \frac{\cos\theta_h}{\cos\theta_{zh}} + \mathrm{SW_{dif}} \cdot \frac{1+\cos\beta}{2} + \mathrm{SW_{down}} \cdot \alpha_\mathrm{G} \cdot \frac{1-\cos\beta}{2} + \mathrm{SW_{ref}} \cdot \frac{1+\cos\beta}{2}\right) \cdot (1-\alpha_\mathrm{PV}), \quad (2)$$

where α_PV denotes the surface albedo of the PV panel. θ_{zh} represents the solar zenith angle (°); θ_h is the incidence angle on the tilted panel (°); and β denotes the panel tilt angle (°). $\mathrm{SW_{dir}}$, $\mathrm{SW_{dif}}$, and $\mathrm{SW_{down}}$ are the beam, diffuse, and total incoming shortwave radiation fluxes (W m^{-2}), respectively; $\mathrm{SW_{ref}}$ denotes the ground-reflected shortwave radiation (W m^{-2}), which is parameterized as:

$$\mathrm{SW_{ref}} = \mathrm{SW_{down}} \cdot \alpha_\mathrm{G} \cdot (1 - f_\mathrm{PV}) \quad (3)$$

α_G is the surface albedo of the underlying ground. f_PV is the fractional surface coverage of PV panels is used as an approximation of the shaded area fraction (Masson et al., 2014).

$\mathrm{LW^*_{PV}}$ is determined by the difference between the incoming and outgoing radiation at the PV panel, following Wallace and Hobbs (2006). The incoming longwave radiation is calculated by considering the contributions from the sky, ground, and neighboring PV panels, while the outgoing term consists of radiation emitted from the front and rear surfaces of the PV panel. $\mathrm{LW^*_{PV}}$ is given by:

$$\begin{aligned}\mathrm{LW^*_{PV}} = {} & \varepsilon_\mathrm{top} \cdot \mathrm{SVF_{PV}} \cdot \mathrm{LW_{down}} \\ & + \mathrm{GVF_{PV}} \cdot \varepsilon_\mathrm{G} \cdot \sigma \cdot T_\mathrm{G}^4 \\ & + \mathrm{PVF_{PV}} \cdot \varepsilon_\mathrm{top} \cdot \sigma \cdot T_\mathrm{PV}^4 + \mathrm{PVF_{PV}} \cdot \varepsilon_\mathrm{btm} \cdot \sigma \cdot T_\mathrm{PV}^4 \\ & - \varepsilon_\mathrm{top} \cdot \sigma \cdot T_\mathrm{PV}^4 - \varepsilon_\mathrm{btm} \cdot \sigma \cdot T_\mathrm{PV}^4,\end{aligned} \quad (4)$$

where σ is the Stefan–Boltzmann constant (5.67×10^{-8} W m^{-2} K^{-4}); $\mathrm{LW_{down}}$ denotes the total downward longwave radiation from the atmosphere (W m^{-2}). ε_G, ε_top, and ε_btm denote the emissivities of the ground and the front and rear surfaces of the PV panel, respectively. T_G is the ground surface temperature (K). $\mathrm{SVF_{PV}}$, $\mathrm{PVF_{PV}}$, and $\mathrm{GVF_{PV}}$ denote the view factor of sky, adjacent PV panels, and ground from PV panels, respectively, which can be calculated following the geometric method described in Heusinger et al. (2020).

The sensible heat flux is calculated as:

$$Q_{H,\mathrm{PV}} = 2h_c(T_\mathrm{PV} - T_\mathrm{A}), \quad (5)$$

where h_c (W m^{-2} K^{-1}) denotes the convective heat transfer coefficient and T_A denotes the ambient air temperature (K). The factor of two accounts for the front and rear surfaces of the panel participating in convective heat exchange with the atmosphere. The value of h_c follows the empirical formulations reviewed by Heusinger et al. (2020).

The electrical power generation is estimated following Heusinger et al. (2020):

$$P_\mathrm{out} = \mathrm{SW_{cell}} \cdot \mathrm{Eff_{PV}} \cdot \min[1, 1 - 0.005(T_\mathrm{PV} - 298.15)], \quad (6)$$

where $\mathrm{Eff_{PV}}$ represents the maximum conversion efficiency under the reference condition (1000 W m^{-2}, 25 °C) and $\mathrm{SW_{cell}}$ represents the shortwave radiation absorbed by the solar cell after transmission through the front glazing layer:

$$\mathrm{SW_{cell}} = M \cdot \left(\mathrm{SW_{dir}} \cdot (\pi\alpha)_\mathrm{dir} \cdot \frac{\cos\theta_h}{\cos\theta_{zh}} + \mathrm{SW_{dif}} \cdot (\pi\alpha)_\mathrm{dif} \cdot \frac{1+\cos\beta}{2} + \mathrm{SW_{down}} \cdot (\pi\alpha)_\mathrm{G} \cdot \alpha_\mathrm{G} \cdot \frac{1-\cos\beta}{2}\right), \quad (7)$$

where the parameters $(\pi\alpha)_\mathrm{dir}$, $(\pi\alpha)_\mathrm{dif}$, $(\pi\alpha)_\mathrm{G}$ represent the transmissivity-absorptance products of the glazing for direct,

https://doi.org/10.5194/egusphere-2026-1311
Preprint. Discussion started: 7 April 2026

diffuse, and ground-reflected shorwave radiation, respectively (Duffie and Beckman, 2013). M accounts for the spectral attenuation of solar radiation with increasing optical air mass (King et al., 2004). The physical parameter settings of the PV model in this study largely followed the measurements reported in Jiang (2021).

2.2 Energy-closed coupling scheme

We proposed a coupling scheme with energy balance closure and integrated the modified PV panel energy balance model into the WRF land surface module. In this scheme, the combined energy balance of the PV-ground system is expressed as the sum of the energy budgets of the PV panels and the ground, weighted by their respective coverage fractions. The energy balance of PV panels is described above (Eq. 1-7) and the ground energy balance can be written as

$$\begin{aligned} &\mathrm{SW_{down}} \cdot (1 - f_{\mathrm{PV}}) \cdot (1 - \alpha_{\mathrm{G}}) + \mathrm{LW_{down}} \cdot \varepsilon_{\mathrm{G}} \cdot (1 - \mathrm{PVF_G}) \\ &+ \varepsilon_{\mathrm{btm}} \cdot \sigma \cdot T_{\mathrm{PV}}^4 \cdot \mathrm{PVF_G} - \varepsilon_{\mathrm{G}} \cdot \sigma \cdot T_{\mathrm{G}}^4 - Q_{H,\mathrm{G}} - \mathrm{LH} - \mathrm{GRDFLX} = 0, \end{aligned} \tag{8}$$

where $Q_{H,\mathrm{G}}$ and LH denote the sensible and latent heat fluxes from the ground surface (W m^{-2}), respectively, and GRDFLX is the ground heat flux (W m^{-2}). $\mathrm{PVF_G}$ represents the view factor of PV panels from the ground, which can be calculated as $\mathrm{PVF_G} = (f_{\mathrm{PV}}/\cos\beta) \cdot \mathrm{GVF_{PV}}$ (Yin et al., 2025).

The total energy balance of the coupled PV-ground system is obtained from the combined PV panel and ground surface energy equation. The thermal capacity of the PV panel is neglected, as Yin et al. (2025) showed that this simplification increases the root-mean-square error (RMSE) of simulated PV surface temperature by only 0.2 °C. The resulting PV-ground system energy balance can be written as:

$$\begin{aligned} &(f_{\mathrm{PV}}/\cos\beta) \cdot [\mathrm{SW_{tot}} \cdot (1 - \alpha_{\mathrm{PV}}) + \mathrm{LW_{PV}^*} - Q_{H,\mathrm{PV}} - P_{\mathrm{out}}] \\ &+[\mathrm{SW_{down}} \cdot (1 - f_{\mathrm{PV}}) \cdot (1 - \alpha_{\mathrm{G}}) + \mathrm{LW_{down}} \cdot \varepsilon_{\mathrm{G}} \cdot (1 - \mathrm{PVF_G}) \\ &+ \varepsilon_{\mathrm{btm}} \cdot \sigma \cdot T_{\mathrm{PV}}^4 \cdot \mathrm{PVF_G} - \varepsilon_{\mathrm{G}} \cdot \sigma \cdot T_{\mathrm{G}}^4 - Q_{H,\mathrm{G}} - \mathrm{LH} - \mathrm{GRDFLX}] = 0, \end{aligned} \tag{9}$$

where $\cos\beta$ converts the inclined PV surface area to its horizontal projection, ensuring that energy fluxes are consistently expressed per unit ground area. After algebraic simplification, the total longwave radiation absorbed by the PV-ground system ($\mathrm{LW_{in}}$) is given by:

$$\mathrm{LW_{in}} = \mathrm{LW_{down}} \cdot [\varepsilon_{\mathrm{top}} \cdot \frac{f_{\mathrm{PV}}}{\cos\beta} \cdot \mathrm{GVF_{PV}} + \varepsilon_{\mathrm{G}} \cdot (1 - \frac{f_{\mathrm{PV}}}{\cos\beta} \cdot \mathrm{GVF_{PV}})], \tag{10}$$

and the total upward longwave radiation of the PV-ground system ($\mathrm{LW_{up}}$) is expressed as

$$\begin{aligned} \mathrm{LW_{up}} = \mathrm{LW_{down}} \cdot \{1 - [\varepsilon_{\mathrm{top}} \cdot \frac{f_{\mathrm{PV}}}{\cos\beta} \cdot \mathrm{GVF_{PV}} + \varepsilon_{\mathrm{G}} \cdot (1 - \frac{f_{\mathrm{PV}}}{\cos\beta} \cdot \mathrm{GVF_{PV}})]\} \\ + \varepsilon_{\mathrm{top}} \cdot \sigma \cdot T_{\mathrm{PV}}^4 \cdot \frac{f_{\mathrm{PV}}}{\cos\beta} \cdot \mathrm{GVF_{PV}} + \varepsilon_{\mathrm{G}} \cdot \sigma \cdot T_{\mathrm{G}}^4 \cdot (1 - \frac{f_{\mathrm{PV}}}{\cos\beta} \cdot \mathrm{GVF_{PV}}). \end{aligned} \tag{11}$$

In this study, an effective emissivity (ε_e) is defined for the PV-ground system as

https://doi.org/10.5194/egusphere-2026-1311
Preprint. Discussion started: 7 April 2026

$$\varepsilon_e = \varepsilon_{\text{top}} \cdot \frac{f_{\text{PV}}}{\cos\beta} \cdot \text{GVF}_{\text{PV}} + \varepsilon_{\text{G}} \cdot (1 - \frac{f_{\text{PV}}}{\cos\beta} \cdot \text{GVF}_{\text{PV}}), \tag{12}$$

and the skin temperature (TSK) is then diagnosed from the emitted longwave flux and the effective emissivity:

$$\text{TSK} = \left(\frac{\varepsilon_{\text{top}} \cdot \sigma \cdot T_{\text{PV}}^4 \cdot \frac{f_{\text{PV}}}{\cos\beta} \cdot \text{GVF}_{\text{PV}} + \varepsilon_{\text{G}} \cdot \sigma \cdot T_{\text{G}}^4 \cdot (1 - \frac{f_{\text{PV}}}{\cos\beta} \cdot \text{GVF}_{\text{PV}}))}{\varepsilon_e \sigma} \right)^{1/4}. \tag{13}$$

The total sensible heat flux emitted by the PV-ground system (SH) is represented by

$$\text{SH} = Q_{H,\text{PV}} \cdot \frac{f_{\text{PV}}}{\cos\beta} + Q_{H,\text{G}}. \tag{14}$$

The scheme ensures energy balance closure among the panels, the ground, and the atmosphere.

3 Data and method

3.1 Data for evaluation

China Meteorological Forcing Dataset Version 2.0 (CMFD) was adopted to evaluate the simulated 2 m air temperature and precipitation. CMFD is a gridded product produced by merging in situ observations, satellite retrievals, and reanalysis fields (He et al., 2020). The spatial and temporal resolutions of the CMFD are 0.1° and 3 hours, respectively, and the dataset covers the period from 1951 to 2024. In addition, station-based observations of daily precipitation were obtained from the National Meteorological Science Data Center of the China Meteorological Administration (CMA), and used to examine the simulated precipitation frequency distribution. In this study, the data from 42 stations were used. MODIS land surface temperature products were applied to assess TSK. We employed the 8-day averaged product at 1 km spatial resolution. Prior to comparison, MODIS pixels flagged as cloudy were excluded.

3.2 PV panels datasets

Three datasets were used to characterize the spatial distribution of PV installations. The first was the China Photovoltaic Power Plant Vector Dataset 2024 (Yang et al., 2025). The second was the Global Photovoltaic Solar Panel Dataset (2019–2022) (Li et al., 2025a). The third was the Photovoltaic Dataset of China (2013–2023), from which the 2018 and 2023 layers were used (Lin, 2024). All three datasets were based on high-resolution satellite imagery, generated using machine learning classification approaches, and validated against manually interpreted samples. To align with the resolution of MODIS land surface temperature dataset, only PV facilities with areas greater than 1 km² were retained.

https://doi.org/10.5194/egusphere-2026-1311
Preprint. Discussion started: 7 April 2026

3.3 Model setting

The WRF model version 4.4.2 (Skamarock et al., 2019) was employed to investigate the effects of utility-scale PV installations on regional climate. WRF is an advanced non-hydrostatic mesoscale model and is widely used in regional climate simulations and land-atmosphere interaction studies. In this study, the PV-ground coupling scheme in Section 2.2 was integrated into WRF. WRF was configured for high-resolution simulations using a two-way nested setup comprising three domains, with horizontal resolutions of 27 km, 9 km, and 3 km, respectively (Fig. 1). All three domains were centered at 38°N, 103°E and consisted of 211×196 grids with the Lambert conformal conic projection. The outermost domain (D01) covered East and Central Asia to capture large-scale circulation features, such as the East Asian summer monsoon, that influence China's regional climate. The intermediate domain (D02) covered several provinces in western China. The innermost domain (D03) covered the major PV concentration region in China to simulate the climatic effects induced by utility-scale PV installations. In the vertical direction, the WRF model was configured with 38 layers, and the top layer was set to 50 hPa.

The physical parameterization schemes applied in the WRF simulations included the Dudhia shortwave radiation scheme (Dudhia, 1989), rapid radiative transfer model (RRTM) longwave radiation scheme (Mlawer et al., 1997), revised MM5 Monin–Obukhov surface layer scheme (Jiménez et al., 2012), Lin microphysics scheme (Chen and Sun, 2002), University of Washington (UW) planetary boundary layer (Bretherton and Park, 2009), and Noah land surface model (Chen and Dudhia, 2001). The Grell 3D ensemble cumulus scheme (Grell and Dévényi, 2002) was activated in all domains.

The ERA5 reanalysis data (Hersbach et al., 2020) were used to provide initial and lateral boundary conditions for the WRF simulations. ERA5 provides surface and pressure-level variables at a 0.25° horizontal resolution and a 3-hourly interval. Additionally, sea surface temperature was obtained from ERA5 and updated daily in the WRF simulations.

3.4 Numerical simulation design

Two sets of WRF simulations were conducted to assess the climatic response to utility-scale PV installations during summer. The first experiment (WRF_PV) included the annual evolution of PV distribution, while the second experiment (WRF_CTL) used the original land-use data without PV installations. In WRF_PV, the PV-ground coupling scheme updated surface temperature and energy fluxes at PV grid cells and enabled an explicit representation of PV-atmosphere feedback. Both simulations employed the model configuration described in Section 3.3. Each simulation ran separately for the period of 2018 to 2024, with simulations initialized on 1 May and terminated on 31 August. The first month (May) was discarded as the model spin-up period, while the remaining three months (June–August) were used for analysis.

https://doi.org/10.5194/egusphere-2026-1311
Preprint. Discussion started: 7 April 2026

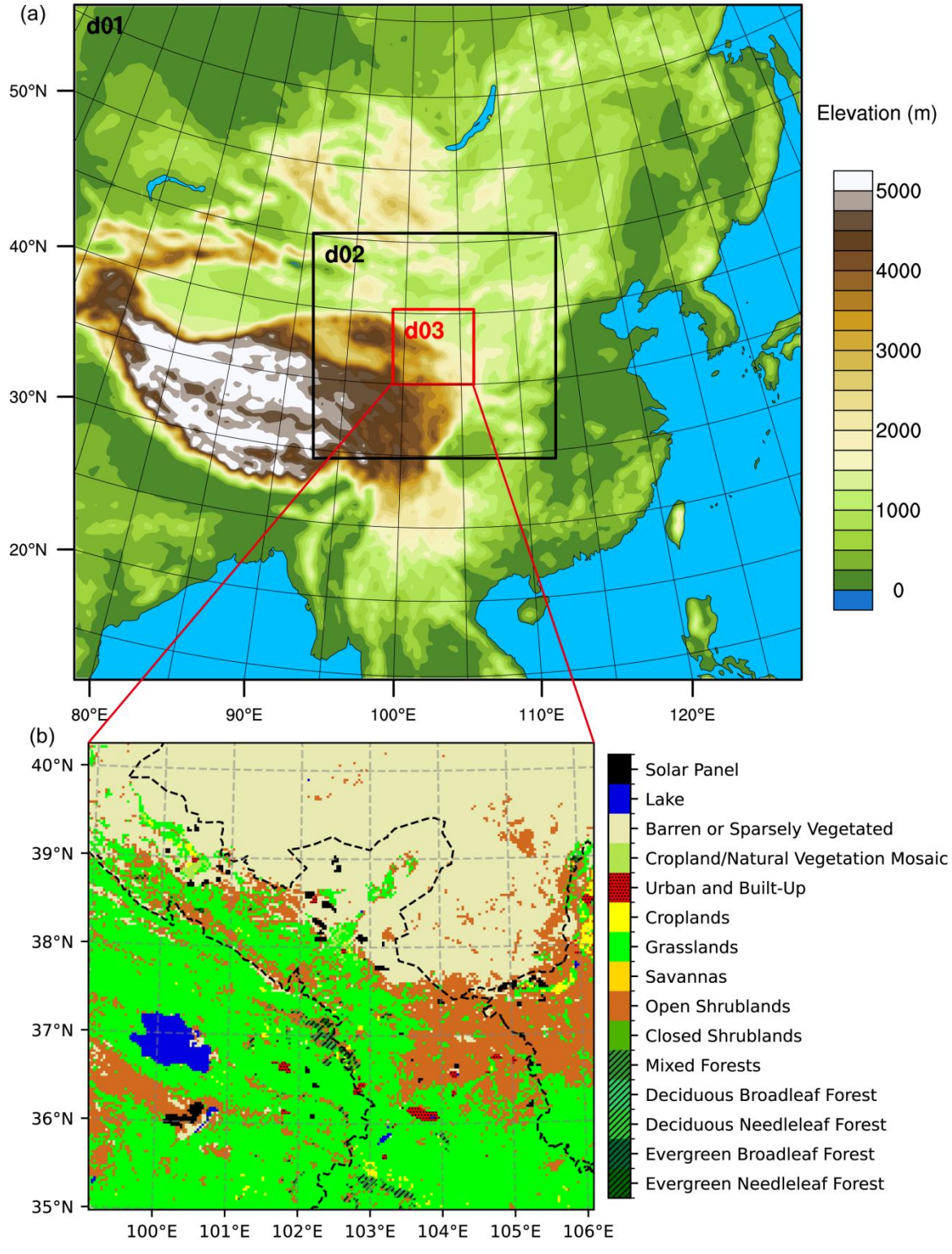

https://doi.org/10.5194/egusphere-2026-1311
Preprint. Discussion started: 7 April 2026

Figure 1: (a) Three nested WRF domains with terrain elevation. (b) Land-use type of D03 in WRF_PV for the year 2024.

4 Result

4.1 Model evaluation

4.1.1 2 m air temperature

The simulated 2 m air temperature (T2) from WRF_PV and WRF_CTL was evaluated against CMFD. CMFD showed horizontal heterogeneity across the study area, with high temperatures over the northern desert regions and low temperatures over the southwestern plateau and mountainous areas (Fig. 2a). Both WRF_PV and WRF_CTL successfully reproduced the spatial variations of T2 across the study region and captured the influence of elevation and underlying surface conditions on the temperature pattern (Fig. 2b and 2c). In addition, Fig. 4 indicates that WRF_PV and WRF_CTL yielded very similar T2 statistics, with correlations of 0.98 and normalized standard deviations of 1.1 relative to CMFD. Figure 2d further compares the diurnal cycle of spatially averaged T2 from CMFD, WRF_PV, and WRF_CTL, showing that both simulations captured the overall temporal evolution well. These results indicate that both experiments reasonably reproduced the regional spatial and temporal characteristics of T2.

https://doi.org/10.5194/egusphere-2026-1311
Preprint. Discussion started: 7 April 2026

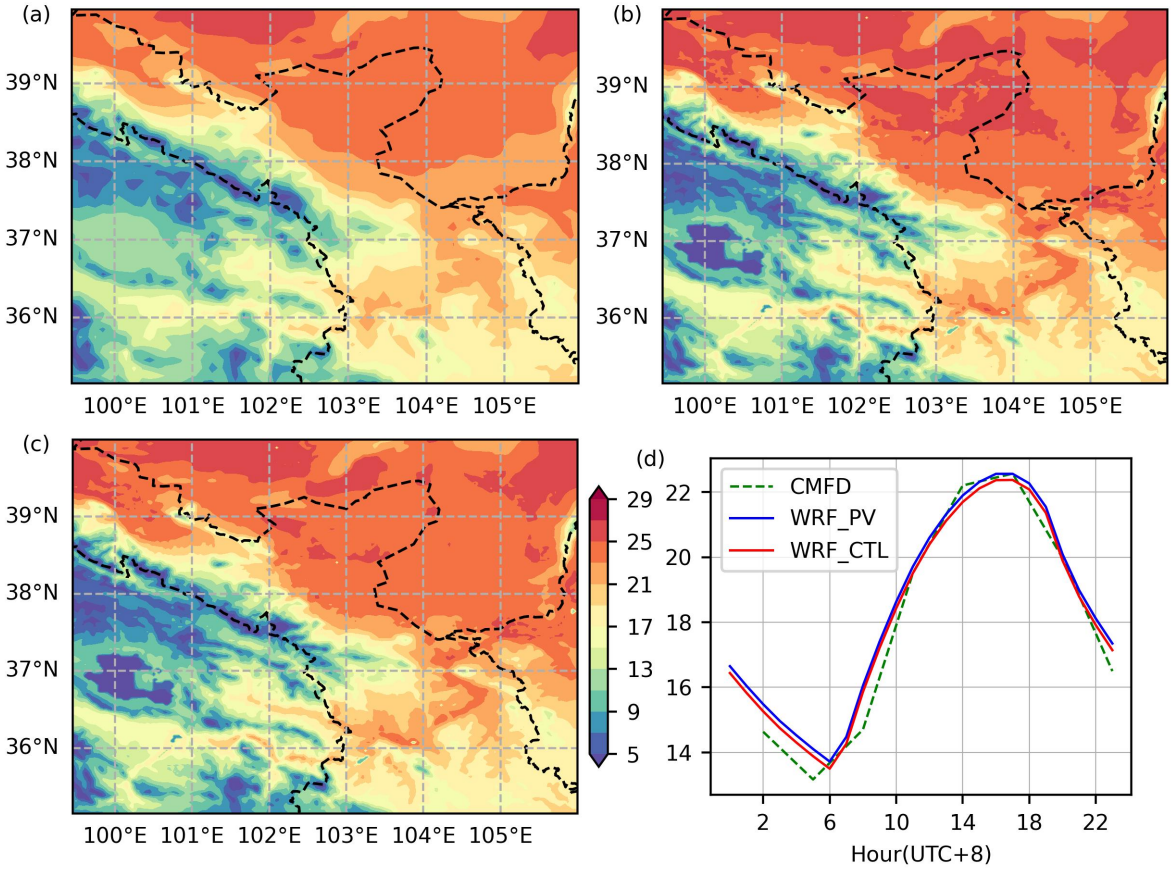

Figure 2: Spatial distribution of mean air temperature at 2 m height (T2, °C) during summer (June, July and August) in D03: (a) CMFD data, (b) WRF_PV simulation and (c) WRF_CTL simulation. (d) Diurnal cycle of T2 averaged over the study area.

4.1.2 Precipitation

Precipitation simulated by both WRF_PV and WRF_CTL was also evaluated using CMFD. As shown in Fig. 3a, the study region exhibited pronounced spatial heterogeneity in precipitation. Daily mean precipitation was below 1 mm in the northern desert regions, whereas it exceeded 3 mm along the plateau margins. Both WRF_PV and WRF_CTL realistically reproduced the regional precipitation pattern and captured monsoonal and topographic effects (Fig. 3b and 3c). Both simulations showed an underestimation of precipitation intensity over the plateau but an overestimation in the southern part of the domain. Nevertheless, Fig. 4 indicates that both WRF_PV and WRF_CTL reproduced the spatial characteristics of precipitation well. WRF_PV yielded a spatial correlation of 0.91 and a normalized standard deviation of 0.91, while WRF_CTL yielded corresponding values of 0.90 and 0.93. Additionally, Figure 3d presents the probability density distribution of daily precipitation derived from CMA station observations, WRF_PV, and WRF_CTL. The observed and simulated precipitation distributions were generally consistent across different intensity ranges. Overall, both experiments

https://doi.org/10.5194/egusphere-2026-1311
Preprint. Discussion started: 7 April 2026

reasonably captured the spatial pattern and the frequency distribution of precipitation, demonstrating their reliability for regional climate.

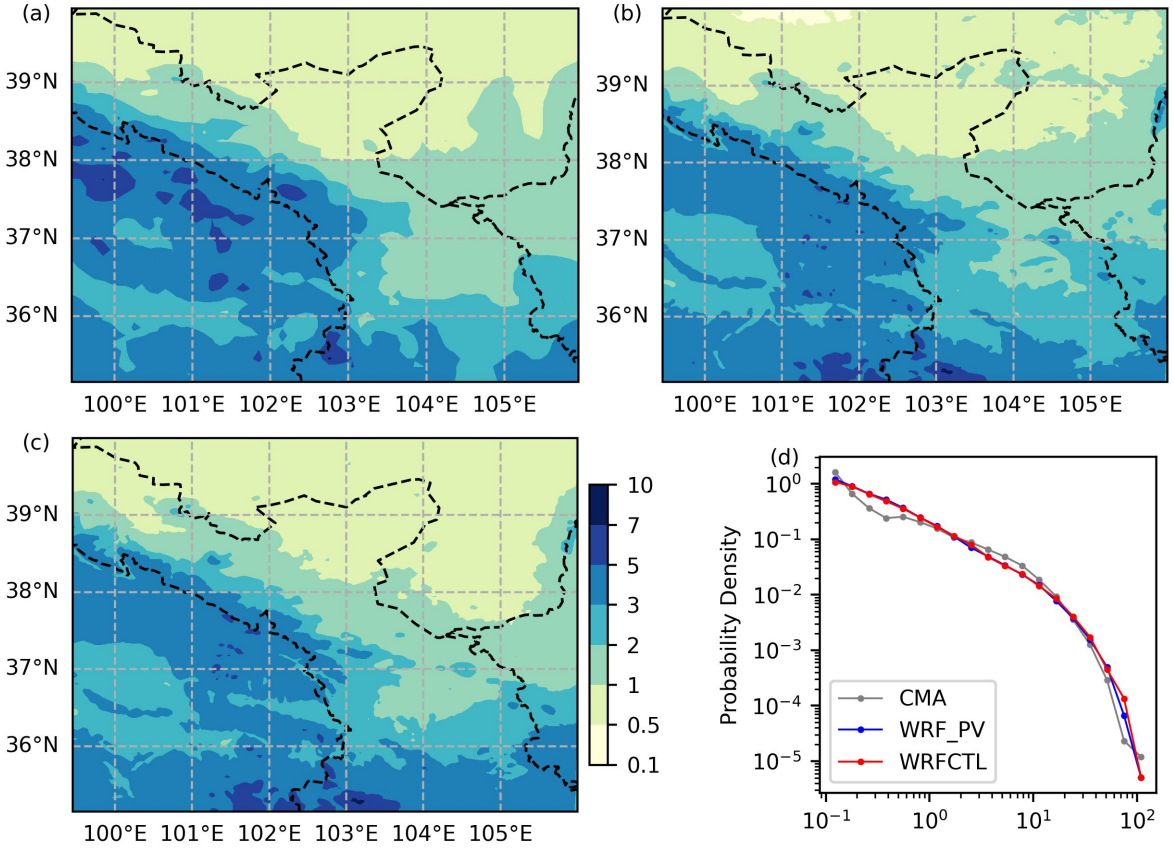

Figure 3: Spatial distribution of mean precipitation (mm day-1) during summer in D03: (a) CMFD data, (b) WRF_PV simulation and (c) WRF_CTL simulation. (d) Probability distribution of daily precipitation intensity derived from CMA station observations (grey line) and from WRF_PV (blue line) and WRF_CTL (red line). Simulation results were interpolated to station points.

https://doi.org/10.5194/egusphere-2026-1311
Preprint. Discussion started: 7 April 2026

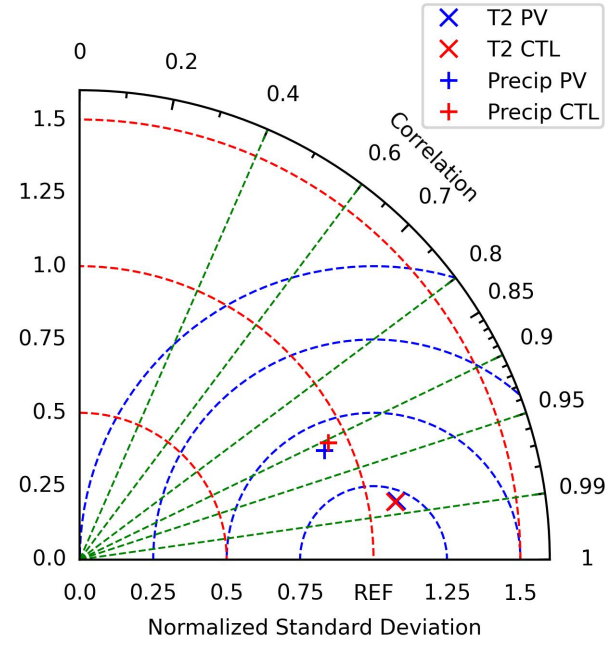

Figure 4: Taylor diagram of T2 and precipitation for WRF_PV and WRF_CTL relative to CMFD.

4.1.3 Simulated skin temperature (TSK)

The performance of TSK simulation was evaluated using MODIS data over the PV grid cells. As shown in Fig. 5, the TSK error distributions of WRF_PV and WRF_CTL were approximately Gaussian and centered around zero, indicating that both simulations captured the overall variability of TSK. However, WRF_PV showed a slightly higher probability density near zero, suggesting better agreement with MODIS compared with WRF_CTL. Quantitatively, the RMSE of TSK decreased from 3.225 °C in WRF_CTL to 3.075 °C in WRF_PV. Therefore, WRF_PV showed improved skill in simulating TSK over PV farms, providing confidence for the subsequent investigation of PV-induced climatic effects.

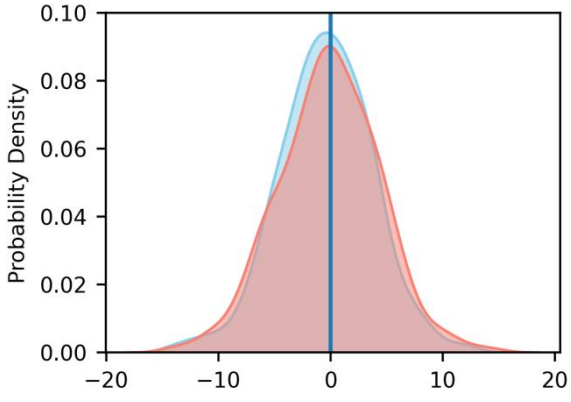

https://doi.org/10.5194/egusphere-2026-1311
Preprint. Discussion started: 7 April 2026

Figure 5: Probability density distributions of skin temperature (TSK, °C) errors for the WRF_PV (blue shade) and WRF_CTL (red shade) simulations with respect to MODIS observations.

4.2 Impacts on local temperature

We compared the diurnal variation of surface temperatures from WRF_PV and WRF_CTL over all PV grids. In WRF_PV, surface temperatures included T_{PV}, T_G, and their integrated skin temperature (TSK_PV) following Eq. (13). In contrast, WRF_CTL included only the land surface skin temperature (TSK_CTL). As shown in Fig. 6a, T_{PV} rose rapidly after sunrise and reached its maximum of 48.8°C at 13:00 (times hereafter are all in local standard time, LST), about one hour earlier than TSK_CTL, which peaked at 14:00. T_{PV} was higher than TSK_CTL during the day and slightly lower after sunset. The earlier peak and larger amplitude resulted from the lower heat capacity of the PV material, which allowed it to warm quickly under solar radiation and cool rapidly after sunset. In contrast, T_G exhibited an opposite response (Fig. 6a). T_G remained slightly lower than TSK_CTL after sunrise due to the shading effect of the PV panels, while it became higher at night as downward longwave radiation from the panels warmed the shaded ground. T_G reached a peak of 35.4°C at 14:00, about 5°C lower than the peak of TSK_CTL.

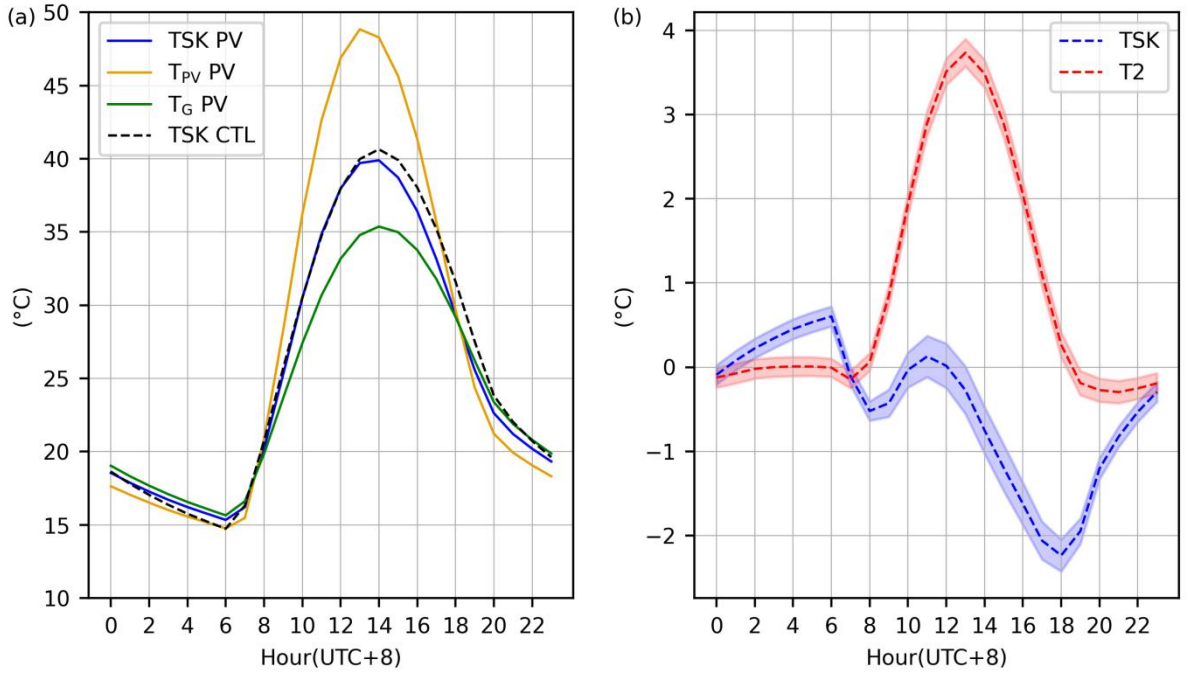

Figure 6: (a) Mean diurnal cycle of skin temperature (TSK_PV), ground surface temperature (T_G PV), surface temperature of PV panels (T_{PV} PV) in WRF_PV and skin temperature in WRF_CTL (TSK_CTL), averaged over all PV grid cells. (b) Diurnal cycle of differences of TSK and T2 between WRF_PV and WRF_CTL. The shaded areas represent the 95% confidence interval based on mean ± 1.96 × standard error.

The combined skin temperature TSK_PV exhibited an intermediate thermal behavior. Its peak temperature appeared at 14:00, consistent with both T_G and TSK_CTL, with a maximum of 39.9°C, which was 0.7°C lower than the control peak

https://doi.org/10.5194/egusphere-2026-1311
Preprint. Discussion started: 7 April 2026

(Fig. 6a). As shown in Fig. 6b, from afternoon to midnight, TSK_PV was significantly lower than TSK_CTL, with the difference reaching up to -2.2 °C at 18:00. The cooling was dominated by T_G, with minor influence from T_{PV}. Between midnight and sunrise, TSK_PV became significantly higher than TSK_CTL, reaching a maximum difference of +0.6 °C at 06:00, driven by the higher T_G. Generally, TSK_PV was lower than TSK_CTL during daytime (08:00 – 19:00), with an average temperature difference of -0.9 ° C. During nighttime (20:00 – 07:00), the temperature difference was negligible, averaging -0.07 °C.

The T2 difference between WRF_PV and WRF_CTL showed a significant daytime warming, averaging +1.8 °C and peaking at +3.5 °C at 13:00 (Fig. 6b). This indicated that the PV panels warmed the near-surface air temperature. At night, the differences were minor, with an average of -0.1°C. Moreover, the diurnal temperature range of the ambient air increased under the PV scenario. Notably, compared with WRF_CTL, WRF_PV exhibited a decrease in TSK but an increase in T2, implying a redistribution of heat between the surface and the lower atmosphere. This differential response motivates a more detailed examination of the radiative processes involved and of how surface energy is partitioned at the land surface.

4.3 Impacts on local energy budget

Figure 7a illustrates that the PV deployment notably altered the daytime radiative balance. The most pronounced feature was a strong reduction in upward shortwave radiation (SW_{up}), reaching up to -97 W m^{-2}, with a daytime average difference of -48 W m^{-2}. An exception occurred shortly after sunrise and before sunset, when SW_{up} showed brief positive anomalies due to specular reflection from the PV panels at large solar zenith angles. Consistent with the differences in SW_{up}, the net radiation (NetRad) showed a pronounced positive anomaly that peaked at 99 W m^{-2}, with a daytime mean increase of 56 W m^{-2}. These changes confirmed that more radiative energy was available at the surface during the day under the PV scenario. The increase in NetRad was also partly attributed to a reduction in upward longwave radiation (LW_{up}), which decreased through most of the day, consistent with the cooler skin temperature and the lower emissivity of the PV panel surface. Overall, the increase in NetRad provided additional available energy at the surface under the PV scenario, driven by the reduced upward shortwave reflection and the diminished upward longwave emission.

https://doi.org/10.5194/egusphere-2026-1311
Preprint. Discussion started: 7 April 2026

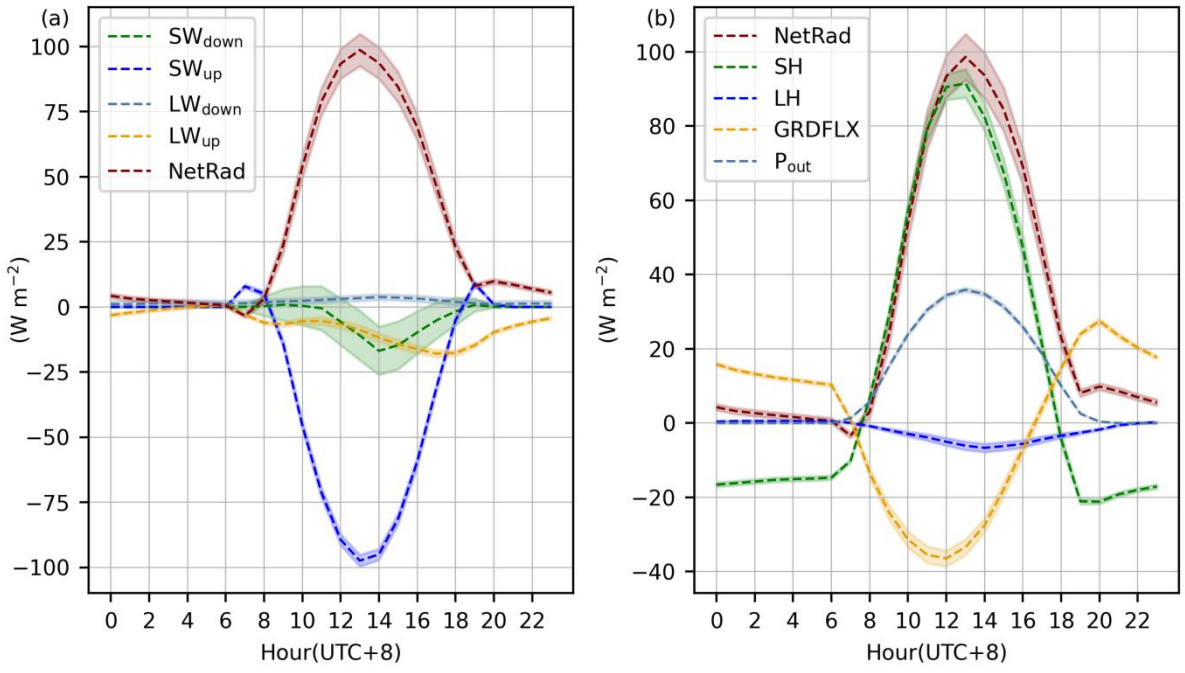

Figure 7: (a) Diurnal cycle of differences of downward shortwave radiation (SW_{down}), upward shortwave radiation (SW_{up}), downward longwave radiation (LW_{down}), upward longwave radiation (LW_{up}), and net radiation (NetRad) between WRF_PV and WRF_CTL, averaged over all PV grid cells. (b) Diurnal cycle of differences of net radiation, sensible heat flux (SH), latent heat flux (LH), ground heat flux (GRDFLX) and electrical power output (P_{out}) between W RF_PV and WRF_CTL, averaged over all PV grid cells. The shaded areas represent the 95% confidence interval based on mean ± 1.96 × standard error.

Figure 7b shows the differences in non-radiative fluxes, averaged over all PV grid cells. Electrical power output peaked at 36 W m^{-2}, with a daytime mean of 22 W m^{-2}. This energy conversion represented an anthropogenic sink of surface energy and reduced the fraction of absorbed radiation that can be released as heat. The sensible heat flux (SH) in WRF_PV increased significantly during daytime, with a maximum difference of 92 W m^{-2} and a daytime mean of 46 W m^{-2}. This increase was attributable to higher T_{PV} and the larger surface area provided by the double-sided panels. This enhancement indicated intensified upward heat transport from the surface into the atmosphere, which contributed to the daytime warming of the ambient air (Fig. 6b). At night, however, SH difference became negative, with an average difference of -16 W m^{-2}, indicating an enhancement of downward sensible heat transfer from the atmosphere to the PV-ground system. When averaged over the entire diurnal cycle, SH showed a positive mean difference of 15 W m^{-2}. The latent heat flux (LH) exhibited an overall decrease under the PV scenario, with a daily mean decrease of about 2 W m^{-2}, corresponding to roughly 8% of total evaporation. This reduction reflected the suppression of surface evaporation caused by panel shading. The ground heat flux (GRDFLX), defined as positive downward, also showed distinct diurnal changes. It decreased during daytime by 15.3 W m^{-2}, indicating that less energy penetrated into the soil due to panel shading. During nighttime, by contrast, GRDFLX became positive by 14.9 W m^{-2}, meaning that the upward release of soil heat toward the surface was weakened. When averaged over the full diurnal cycle, the net change in GRDFLX was nearly zero, reflecting that the

https://doi.org/10.5194/egusphere-2026-1311
Preprint. Discussion started: 7 April 2026

reduced daytime storage was canceled out by the reduced nighttime release. This indicated a decrease in soil heat content and a weaker diurnal heat exchange (Fig. 8). Overall, the PV installation not only increased the total available surface energy but also redistributed it. After PV deployment, energy was shifted from the subsurface to the atmosphere, as sensible heat exchange increased during the day while ground heat storage weakened. This shift reconciled the cooler surface with a warmer near-surface atmosphere.

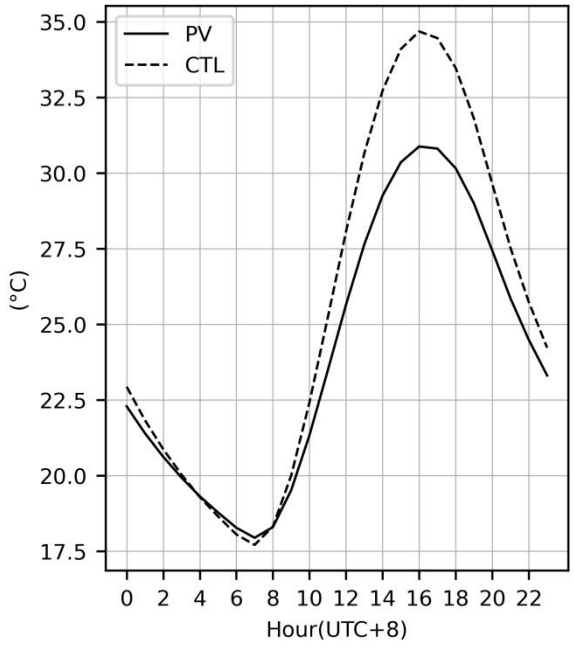

Figure 8: (a) Mean diurnal cycle of the 0-7 cm soil temperature in WRF_PV and WRF_CTL, averaged over all PV grid cells.

Having discussed the surface responses above, we now focus on the atmospheric feedbacks induced by PV installation, as reflected in the downward longwave and shortwave fluxes (LW_{down} and SW_{down}, Fig. 7a). LW_{down} increased slightly, while SW_{down} decreased significantly in the afternoon, with the largest difference of -17 W m^{-2} occurring at 14:00, and a daytime mean difference of -5.2 W m^{-2}. The daytime mean difference accounted for approximately 1% relative to the daytime mean SW_{down} in WRF_CTL. This attenuation indicated that PV deployment affected the local solar resource and surface radiative forcing, with implications for PV yield estimation. The reduction in SW_{down} was due to an increase in low cloud fraction (Fig. 9a). The low cloud fraction anomaly remained slightly positive throughout the day with a significant increase of approximately 1 to 2% in the afternoon, when the decrease in SW_{down} was most pronounced. This rise in low-level clouds was consistent with the changes in vertical velocity and atmospheric stability (Fig. 9b and 9c). The vertical velocity showed positive anomalies (upward motion) between 600 and 850 hPa during 10:00–16:00, indicating locally intensified lifting driven by PV-induced enhanced sensible heat flux over the PV-covered area. Consistently, the static stability difference showed negative anomalies below about 600 hPa during daytime, reflecting reduced stability associated

https://doi.org/10.5194/egusphere-2026-1311
Preprint. Discussion started: 7 April 2026

with the intensified thermal convection. Therefore, PV deployment not only shifted the surface energy partitioning but also changed the radiative energy input through land–atmosphere feedbacks,.

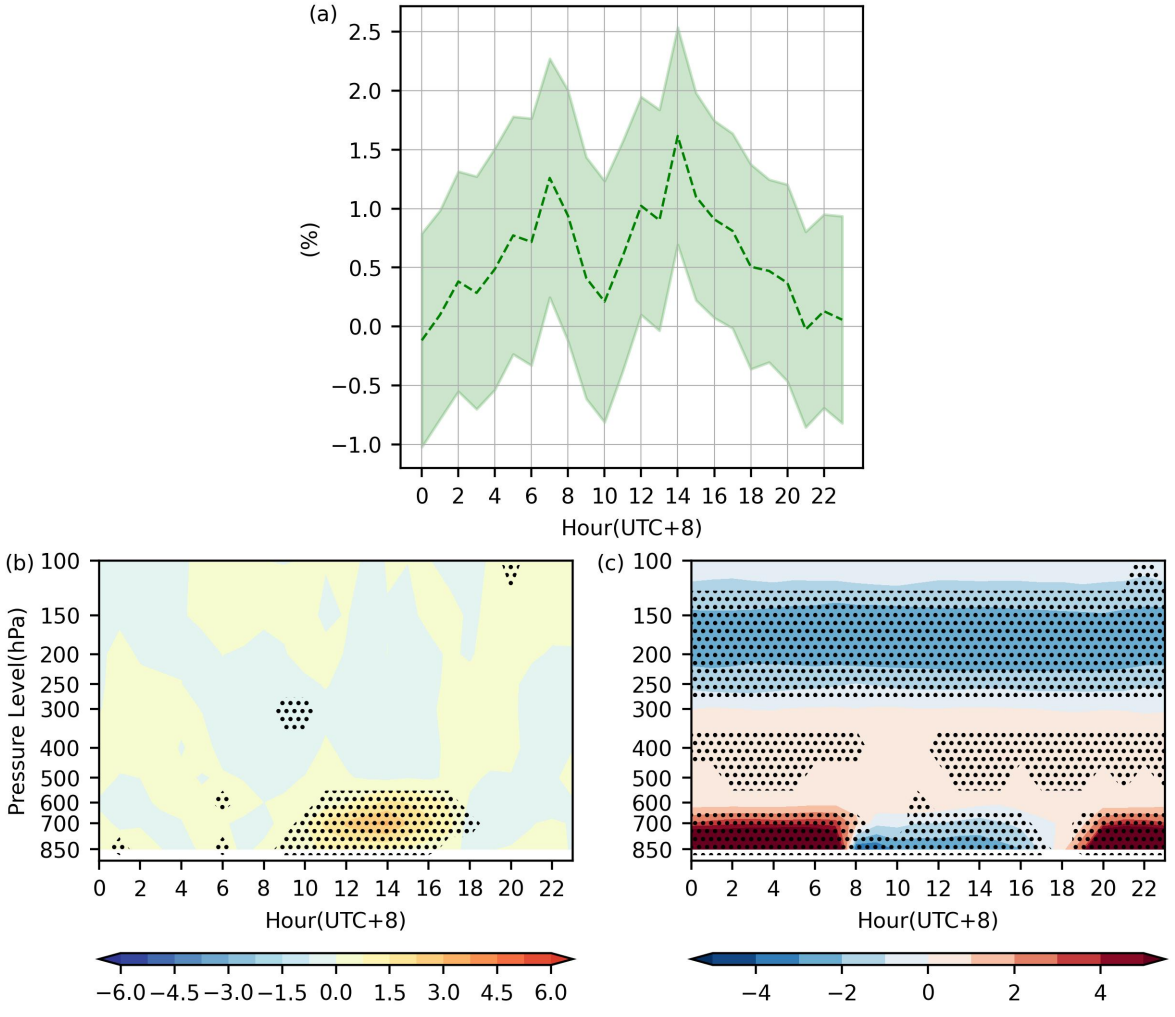

Figure 9: Mean diurnal cycle of the difference of (a) low cloud fraction (below 600 hPa), (b) vertical velocity (cm s^{-1}) and (c) static stability (10^{-4} K m^{-1}) between WRF_PV and WRF_CTL, averaged over all PV grid cells. The shaded area in (a) and dotted portions in (b) and (c) represent the 95% confidence interval based on mean ± 1.96 × standard error.

4.4 Impacts on precipitation

Figure 10 shows the distribution of quantile-based differences in precipitation between WRF_PV and WRF_CTL over the PV farms and surrounding areas (D03 in Fig. 1). Overall, the median values remained close to zero below the 60th percentile, indicating that PV deployment exerted little influence on light rainfall. From the 60th to 95th percentile, the differences turned negative. In contrast, precipitation above the 95th percentile exhibited a pronounced positive shift, with about 64% of grid points showing an increase. This contrasting pattern indicated that PV panels may reduce moderate

https://doi.org/10.5194/egusphere-2026-1311
Preprint. Discussion started: 7 April 2026

precipitation but intensify extreme precipitation events, although the regional-mean total precipitation showed little change (not shown). Moreover, the increased share of extreme precipitation occurred across many more grid cells than those covered by PV. Hence, PV forcing triggered a nonlocal intensification of extreme precipitation.

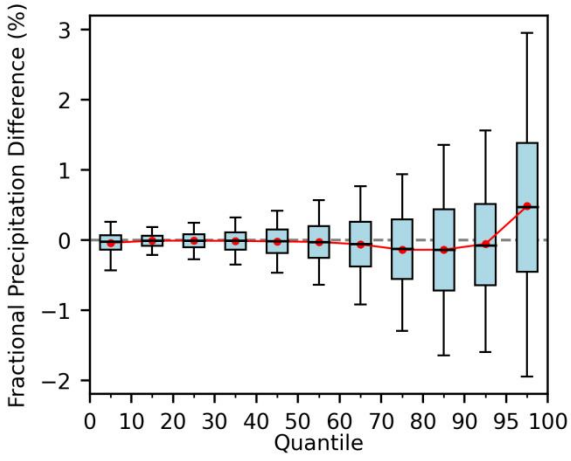

Figure 10: Quantile-based differences in total precipitation between WRF_PV and WRF_CTL in D03. For each grid point, precipitation amounts within the 10th, 20th, …, and 95th quantile intervals were summed and expressed as fractions of the 7 year cumulative precipitation. The differences in these fractions (WRF_PV minus WRF_CTL) were then computed for each grid point and summarized across all grid points to obtain the distribution of changes in precipitation contribution for different intensity categories.

5 Conclusions and Discussion

In this study, we developed a coupled WRF-PV model and applied it to summer conditions in northwestern China to assess the regional climatic impacts of utility-scale PV installations. The coupling maintains surface energy balance closure between PV arrays and the underlying ground. This model provides a unified, physically consistent land–atmosphere framework for resolving PV-induced changes in surface energy balance and atmospheric response.

Evaluations showed that our model captured the spatial patterns of temperature and precipitation, the diurnal temperature cycle, and the precipitation frequency distribution. Moreover, the inclusion of the PV model improved the simulation of the skin temperature over PV farms, yielding a lower RMSE than WRF_CTL. During daytime, PV installations cooled the skin temperature (mean 0.9°C, maximum 2.2 °C). This cooling is consistent with multiple remote sensing analyses of PV farms, which reported surface cooling of about 0.5 to 2 °C (Zhang and Xu, 2020; Fan and Huang, 2021; Guoqing et al., 2021; Wang et al., 2024; Xu et al., 2024). Furthermore, PV deployment increased sensible heat flux while reducing latent heat and ground heat fluxes in the daytime, in good agreement with site measurements (Broadbent et al., 2019; Jiang et al., 2021). The enhanced sensible heating arose from increased net radiation and reduced latent and ground heat fluxes. Consequently, daytime 2 m air temperature increased (mean 1.8 °C, maximum 3.5 °C). This result is comparable to the near-surface warming of about 0.2 to 2.6 °C reported in previous site measurements (Barron-Gafford et al.,

https://doi.org/10.5194/egusphere-2026-1311
Preprint. Discussion started: 7 April 2026

2016; Yang et al., 2017; Broadbent et al., 2019; Wu et al., 2020; Jiang et al., 2021; Li et al., 2023; Zhang et al., 2024). Additionally, enhanced sensible heating reduced lower atmospheric stability and promoted upward motion, increasing low-level cloud fraction and thereby weakening incoming shortwave radiation. PV installations also affected regional precipitation, reducing moderate rainfall and increasing extreme events.

Several previous numerical studies reported similar PV-induced effects, including higher air temperature and increased cloud fraction (Li et al., 2018; Lu et al., 2021; Long et al., 2024). Yet the magnitudes of these changes were much larger than those in our simulations. A key reason is that these simulations assigned an effective albedo to the entire grid cell to represent PV installations. In reality, PV panels occupy only part of the grid cell, so the panel effective albedo should be area-weighted with the albedo of the exposed ground between the rows. By neglecting the space between PV rows, the approach exaggerated the albedo contrast and the resulting radiative forcing. In addition, these studies neglected the low heat capacity of PV panels and the removal of energy from the subsurface, even though both mechanisms would induce a pronounced diurnal cycle in PV thermal effects and limit the persistence of warming. As a result, these simulations yielded stronger atmospheric responses. By contrast, our WRF-PV model explicitly represented panel coverage fraction, panel thermal properties and shading effects, leading to results closer to observations. As for precipitation, previous experiments using the effective albedo method generally reported increases in total precipitation (Li et al., 2018; Lu et al., 2021), whereas our simulation showed little change in total precipitation but a redistribution toward extreme precipitation.

However, this study considered only the evaporation change, without examining other hydrological processes including soil moisture variability and vegetation changes, and the potential effect of the panel cleaning process was not included (Yavari et al., 2022). In the future, a coupled land–atmosphere–ecosystem model should be developed to evaluate the impacts of utility-scale PV development on ecosystem processes, including agricultural responses (Weselek et al., 2019). Despite these limitations, this study provided a framework to assess how utility-scale PV installations influence surface energy balance, land–atmosphere interactions, and regional climate.

Code, data, or code and data availability

The WRF-PV model code, configuration files, and processed datasets used in this study are archived at Zenodo and are publicly available at: https://doi.org/10.5281/zenodo.18919333 (Chen, 2026). The PV module was implemented based on version 4.4.2 of the WRF (Skamarock et al., 2019), which is publicly available from the WRF official repository: https://github.com/wrf-model/WRF/tree/release-v4.4.2. The MODIS land surface temperature data used for model evaluation are available from the NASA Earthdata archive (https://earthdata.nasa.gov). The China Meteorological Forcing Dataset (He et al., 2020) is publicly available from the National Tibetan Plateau Data Center (https://data.tpdc.ac.cn).

https://doi.org/10.5194/egusphere-2026-1311
Preprint. Discussion started: 7 April 2026

Author contributions

JJ conceived the study. YC developed the methodology and software, carried out the investigation, performed the formal analysis, prepared the visualizations, and wrote the original draft. JJ and YL supervised the research. JH contributed to the software development. JJ, YL, JH, JC, and ZZ reviewed and edited the manuscript. YL acquired the funding.

Competing interests

The contact author has declared that none of the authors has any competing interests.

Acknowledgements

We thank Prof. Scott Krayenhoff at University of Guelph for his valuable guidance on the photovoltaic panel energy balance code.

Financial support

This study was supported by the National Natural Science Foundation of China (Grant No. 42288101).

References

Armstrong, A., Ostle, N. J., and Whitaker, J.: Solar park microclimate and vegetation management effects on grassland carbon cycling, Environ. Res. Lett., 11, 074016, https://doi.org/10.1088/1748-9326/11/7/074016, 2016.

Barron-Gafford, G. A., Minor, R. L., Allen, N. A., Cronin, A. D., Brooks, A. E., and Pavao-Zuckerman, M. A.: The Photovoltaic Heat Island Effect: Larger solar power plants increase local temperatures, Sci. Rep., 6, 35070, https://doi.org/10.1038/srep35070, 2016.

Bretherton, C. S. and Park, S.: A New Moist Turbulence Parameterization in the Community Atmosphere Model, J. Clim., 22, 3422–3448, https://doi.org/10.1175/2008JCLI2556.1, 2009.

Broadbent, A. M., Krayenhoff, E. S., Georgescu, M., and Sailor, D. J.: The Observed Effects of Utility-Scale Photovoltaics on Near-Surface Air Temperature and Energy Balance, J. Appl. Meteorol. Climatol., 58, 989–1006, https://doi.org/10.1175/JAMC-D-18-0271.1, 2019.

Chang, R., Shen, Y., Luo, Y., Wang, B., Yang, Z., and Guo, P.: Observed surface radiation and temperature impacts from the large-scale deployment of photovoltaics in the barren area of Gonghe, China, Renew. Energy, 118, 131–137, https://doi.org/10.1016/j.renene.2017.11.007, 2018.

Chang, R., Luo, Y., and Zhu, R.: Simulated local climatic impacts of large-scale photovoltaics over the barren area of Qinghai, China, Renew. Energy, 145, 478–489, https://doi.org/10.1016/j.renene.2019.06.059, 2020.

https://doi.org/10.5194/egusphere-2026-1311
Preprint. Discussion started: 7 April 2026

Chang, R., Yan, Y., Luo, Y., Xiao, C., Wu, C., Jiang, J., and Shi, W.: A coupled WRF-PV mesoscale model simulating the near-surface climate of utility-scale photovoltaic plants, Sol. Energy, 245, 278–289, https://doi.org/10.1016/j.solener.2022.09.023, 2022.

Chen, Y.: Data and code for the article "Simulating the impacts of utility-scale photovoltaic installations with a physically based coupled WRF–PV model" (Version 1.0), Zenodo [code], https://doi.org/10.5281/zenodo.18919333, 2026.

Chen, F. and Dudhia, J.: Coupling an advanced land surface-hydrology model with the Penn State–NCAR MM5 modeling system. Part I: Model implementation and sensitivity, Mon. Weather Rev., 129, 587–604, https://doi.org/10.1175/1520-0493(2001)129<0569:CAALSH>2.0.CO;2, 2001.

Chen, S.-H. and Sun, W.-Y.: A One-dimensional Time Dependent Cloud Model, J. Meteorol. Soc. Jpn. Ser II, 80, 99–118, https://doi.org/10.2151/jmsj.80.99, 2002.

Coimbra, C. F. M.: Energy Meteorology for the Evaluation of Solar Farm Thermal Impacts on Desert Habitats, Adv. Atmospheric Sci., 42, 313–326, https://doi.org/10.1007/s00376-024-4242-3, 2025.

Dudhia, J.: Numerical study of convection observed during the winter monsoon experiment using a mesoscale two-dimensional model, J. Atmos. Sci., 46, 3077–3107, https://doi.org/10.1175/1520-0469(1989)046<3077:NSOCOD>2.0.CO;2, 1989.

Duffie, J. A. and Beckman, W. A.: Solar Engineering of Thermal Processes, 4th ed., John Wiley & Sons, Inc., 213pp., https://doi.org/10.1002/9781118671603, 2013.

Fan, C. and Huang, X.: Satellite-observed changes of surface spectral reflectances due to solar farming and the implication for radiation budget, Environ. Res. Lett., 15, 114047, https://doi.org/10.1088/1748-9326/abbdea, 2020.

Fan, C. and Huang, X.: Direct impact of solar farm deployment on surface longwave radiation, Environ. Res. Commun., 3, 125006, https://doi.org/10.1088/2515-7620/ac40f1, 2021.

Grell, G. A. and Dévényi, D.: A generalized approach to parameterizing convection combining ensemble and data assimilation techniques, Geophys. Res. Lett., 29, https://doi.org/10.1029/2002GL015311, 2002.

Guoqing, L., Hernandez, R. R., Blackburn, G. A., Davies, G., Hunt, M., Whyatt, J. D., and Armstrong, A.: Ground-mounted photovoltaic solar parks promote land surface cool islands in arid ecosystems, Renew. Sustain. Energy Transit., 1, 100008, https://doi.org/10.1016/j.rset.2021.100008, 2021.

Haegel, N. M., Atwater, H., Barnes, T., Breyer, C., Burrell, A., Chiang, Y.-M., De Wolf, S., Dimmler, B., Feldman, D., Glunz, S., Goldschmidt, J. C., Hochschild, D., Inzunza, R., Kaizuka, I., Kroposki, B., Kurtz, S., Leu, S., Margolis, R., Matsubara, K., Metz, A., Metzger, W. K., Morjaria, M., Niki, S., Nowak, S., Peters, I. M., Philipps, S., Reindl, T., Richter, A., Rose, D., Sakurai, K., Schlatmann, R., Shikano, M., Sinke, W., Sinton, R., Stanbery, B. J., Topic, M., Tumas, W., Ueda, Y., Van De Lagemaat, J., Verlinden, P., Vetter, M., Warren, E., Werner, M., Yamaguchi, M., and Bett, A. W.: Terawatt-scale photovoltaics: Transform global energy, Science, 364, 836–838, https://doi.org/10.1126/science.aaw1845, 2019.

Hasan, A., Alnoman, H., and Rashid, Y.: Impact of integrated photovoltaic-phase change material system on building energy efficiency in hot climate, Energy Build., 130, 495–505, https://doi.org/10.1016/j.enbuild.2016.08.059, 2016.

He, J., Yang, K., Tang, W., Lu, H., Qin, J., Chen, Y., and Li, X.: The first high-resolution meteorological forcing dataset for land process studies over China, Sci. Data, 7, 25, https://doi.org/10.1038/s41597-020-0369-y, 2020.

https://doi.org/10.5194/egusphere-2026-1311
Preprint. Discussion started: 7 April 2026

Hersbach, H., Bell, B., Berrisford, P., Hirahara, S., Horányi, A., Muñoz-Sabater, J., Nicolas, J., Peubey, C., Radu, R., Schepers, D., Simmons, A., Soci, C., Abdalla, S., Abellan, X., Balsamo, G., Bechtold, P., Biavati, G., Bidlot, J., Bonavita, M., De Chiara, G., Dahlgren, P., Dee, D., Diamantakis, M., Dragani, R., Flemming, J., Forbes, R., Fuentes, M., Geer, A., Haimberger, L., Healy, S., Hogan, R. J., Hólm, E., Janisková, M., Keeley, S., Laloyaux, P., Lopez, P., Lupu, C., Radnoti, G., De Rosnay, P., Rozum, I., Vamborg, F., Villaume, S., and Thépaut, J.: The ERA5 global reanalysis, Q. J. R. Meteorol. Soc., 146, 1999–2049, https://doi.org/10.1002/qj.3803, 2020.

Heusinger, J., Broadbent, A. M., Sailor, D. J., and Georgescu, M.: Introduction, evaluation and application of an energy balance model for photovoltaic modules, Sol. Energy, 195, 382–395, https://doi.org/10.1016/j.solener.2019.11.041, 2020.

Heusinger, J., Broadbent, A. M., Krayenhoff, E. S., and Weber, S.: Adaptation of a photovoltaic energy balance model for rooftop applications, Build. Environ., 192, 107628, https://doi.org/10.1016/j.buildenv.2021.107628, 2021.

Hu, A., Levis, S., Meehl, G. A., Han, W., Washington, W. M., Oleson, K. W., Van Ruijven, B. J., He, M., and Strand, W. G.: Impact of solar panels on global climate, Nat. Clim. Change, 6, 290–294, https://doi.org/10.1038/nclimate2843, 2016.

IRENA: Future of solar photovoltaic: deployment, investment, technology, grid integration and socio-economic aspects, International Renewable Energy Agency, Abu Dhabi, ISBN 978-92-9260-156-0, 2019.

IRENA: Renewable capacity statistics 2023, International Renewable Energy Agency, Abu Dhabi, ISBN 978-92-9260-525-4, 2023.

Jiang, J., Gao, X., Lv, Q., Li, Z., and Li, P.: Observed impacts of utility-scale photovoltaic plant on local air temperature and energy partitioning in the barren areas, Renew. Energy, 174, 157–169, https://doi.org/10.1016/j.renene.2021.03.148, 2021.

Jiménez, P. A., Dudhia, J., González-Rouco, J. F., Navarro, J., Montávez, J. P., and García-Bustamante, E.: A Revised Scheme for the WRF Surface Layer Formulation, Mon. Weather Rev., 140, 898–918, https://doi.org/10.1175/MWR-D-11-00056.1, 2012.

King, D., Kratochvil, J., and Boyson, W.: Photovoltaic array performance model., https://doi.org/10.2172/919131, 2004.

Li, A., Liu, L., Li, S., Cui, X., Chen, X., and Cao, X.: Global photovoltaic solar panel dataset from 2019 to 2022, Sci. Data, 12, 637, https://doi.org/10.1038/s41597-025-04985-y, 2025a.

Li, B., Lei, C., Zhang, W., Olawoore, V. S., and Shuai, Y.: Numerical model study on influences of photovoltaic plants on local microclimate, Renew. Energy, 221, 119551, https://doi.org/10.1016/j.renene.2023.119551, 2024.

Li, B., Lei, C., Zhang, W., Xu, J., and Shuai, Y.: A numerical simulation study of microclimate in PV power plant using coupled WRF-PVCM, Energy, 317, 134529, https://doi.org/10.1016/j.energy.2025.134529, 2025b.

Li, P., Luo, Y., He, Z., Zheng, J., Xia, X., Liao, Z., and Gao, X.: A comparative study of the effects of photovoltaic power plants in desert and lake on the microclimate, Energy Rep., 10, 2128–2137, https://doi.org/10.1016/j.egyr.2023.08.064, 2023.

Li, Y., Kalnay, E., Motesharrei, S., Rivas, J., Kucharski, F., Kirk-Davidoff, D., Bach, E., and Zeng, N.: Climate model shows large-scale wind and solar farms in the Sahara increase rain and vegetation, Science, 361, 1019–1022, https://doi.org/10.1126/science.aar5629, 2018.

Li, Z., Zhao, Y., Luo, Y., Yang, L., Li, P., Jin, X., Jiang, J., Liu, R., and Gao, X.: A comparative study on the surface radiation characteristics of photovoltaic power plant in the Gobi desert, Renew. Energy, 182, 764–771, https://doi.org/10.1016/j.renene.2021.10.054, 2022.

https://doi.org/10.5194/egusphere-2026-1311
Preprint. Discussion started: 7 April 2026

Lin, G.: Photovoltaic dataset of China from 2013 to 2023 for ten years, https://doi.org/10.57760/sciencedb.15684, 2024.

Long, J., Lu, Z., Miller, P. A., Pongratz, J., Guan, D., Smith, B., Zhu, Z., Xu, J., and Zhang, Q.: Large-scale photovoltaic solar farms in the Sahara affect solar power generation potential globally, Commun. Earth Environ., 5, 11, https://doi.org/10.1038/s43247-023-01117-5, 2024.

Lu, Z., Zhang, Q., Miller, P. A., Zhang, Q., Berntell, E., and Smith, B.: Impacts of Large-Scale Sahara Solar Farms on Global Climate and Vegetation Cover, Geophys. Res. Lett., 48, e2020GL090789, https://doi.org/10.1029/2020GL090789, 2021.

Lyu, X., Li, X., Wei, H., Wu, J., Dang, D., Zhang, C., Wang, K., and Lou, A.: Mapping of Utility-Scale Solar Panel Areas From 2000 to 2022 in China Using Google Earth Engine, IEEE J. Sel. Top. Appl. Earth Obs. Remote Sens., 17, 18083–18095, https://doi.org/10.1109/JSTARS.2024.3468627, 2024a.

Lyu, X., Li, X., Zhang, C., Dang, D., Wang, K., and Lou, A.: Mapping the carbon mitigation potential of photovoltaic development in the Gobi and desert regions of China, Energy, 308, 132936, https://doi.org/10.1016/j.energy.2024.132936, 2024b.

Masson, V., Bonhomme, M., Salagnac, J.-L., Briottet, X., and Lemonsu, A.: Solar panels reduce both global warming and urban heat island, Front. Environ. Sci., 2, https://doi.org/10.3389/fenvs.2014.00014, 2014.

Mlawer, E. J., Taubman, S. J., Brown, P. D., Iacono, M. J., and Clough, S. A.: Radiative transfer for inhomogeneous atmospheres: RRTM, a validated correlated-k model for the longwave, J. Geophys. Res. Atmospheres, 102, 16663–16682, https://doi.org/10.1029/97JD00237, 1997.

Skamarock, W. C., Klemp, J. B., Dudhia, J., Gill, D. O., Liu, Z., Berner, J., Wang, W., Powers, J. G., Duda, M. G., Barker, D. M., and Huang, X.-Y.: A Description of the Advanced Research WRF Model Version 4, https://doi.org/10.5065/1DFH-6P97, 2019.

Wallace, J. M. and Hobbs, P. V.: Atmospheric science: an introductory survey, 2nd ed., Academic press, Amsterdam Paris, 395pp., https://doi.org/10.1016/C2009-0-00034-8, 2006.

Wang, X., Zhou, Q., Zhang, Y., Liu, X., Liu, J., Chen, S., Wang, X., and Wu, J.: Diurnal Asymmetry Effects of Photovoltaic Power Plants on Land Surface Temperature in Gobi Deserts, Remote Sens., 16, 1711, https://doi.org/10.3390/rs16101711, 2024.

Wei, S., Ziegler, A. D., Qin, Y., Wang, D., Chen, Y., Yan, J., and Zeng, Z.: Small reduction in land surface albedo due to solar panel expansion worldwide, Commun. Earth Environ., 5, 474, https://doi.org/10.1038/s43247-024-01619-w, 2024.

Weselek, A., Ehmann, A., Zikeli, S., Lewandowski, I., Schindele, S., and Högy, P.: Agrophotovoltaic systems: applications, challenges, and opportunities. A review, Agron. Sustain. Dev., 39, 35, https://doi.org/10.1007/s13593-019-0581-3, 2019.

Wu, W., Yue, S., Zhou, X., Guo, M., Wang, J., Ren, L., and Yuan, B.: Observational Study on the Impact of Large-Scale Photovoltaic Development in Deserts on Local Air Temperature and Humidity, Sustainability, 12, 3403, https://doi.org/10.3390/su12083403, 2020.

Xu, Z., Li, Y., Qin, Y., and Bach, E.: A global assessment of the effects of solar farms on albedo, vegetation, and land surface temperature using remote sensing, Sol. Energy, 268, 112198, https://doi.org/10.1016/j.solener.2023.112198, 2024.

https://doi.org/10.5194/egusphere-2026-1311
Preprint. Discussion started: 7 April 2026

Yang, L., Gao, X., Lv, F., Hui, X., Ma, L., and Hou, X.: Study on the local climatic effects of large photovoltaic solar farms in desert areas, Sol. Energy, 144, 244–253, https://doi.org/10.1016/j.solener.2017.01.015, 2017.

Yang, Y., Lin, S., Lu, R., and Liu, X.: CPVPD-2024: A Chinese photovoltaic plant dataset derived via a topography-enhanced deep learning framework, Sci. Data, 12, 1601, https://doi.org/10.1038/s41597-025-05891-z, 2025.

Yavari, R., Zaliwciw, D., Cibin, R., and McPhillips, L.: Minimizing environmental impacts of solar farms: a review of current science on landscape hydrology and guidance on stormwater management, Environ. Res. Infrastruct. Sustain., 2, 032002, https://doi.org/10.1088/2634-4505/ac76dd, 2022.

Yin, H., Krayenhoff, E. S., Voogt, J., Heusinger, J., and Aliabadi, A. A.: Simulation of Tilted Rooftop Photovoltaic Panels at City Scale: Novel Measurements, Model Development, and Application in WRF, J. Geophys. Res. Atmospheres, 130, e2024JD043133, https://doi.org/10.1029/2024JD043133, 2025.

Ying, J., Li, Z., Yang, L., Jiang, Y., Luo, Y., and Gao, X.: The characteristics and parameterizations of the surface albedo of a utility-scale photovoltaic plant in the Gobi Desert, Theor. Appl. Climatol., 151, 1469–1481, https://doi.org/10.1007/s00704-022-04337-5, 2023.

Yue, S., Guo, M., Zou, P., Wu, W., and Zhou, X.: Effects of photovoltaic panels on soil temperature and moisture in desert areas, Environ. Sci. Pollut. Res., 28, 17506–17518, https://doi.org/10.1007/s11356-020-11742-8, 2021.

Zhang, J., Li, Z., Tao, J., Ge, Y., Zhong, Y., Wang, Y., and Yan, B.: Observed Impacts of Ground-Mounted Photovoltaic Systems on the Microclimate and Soil in an Arid Area of Gansu, China, Atmosphere, 15, 936, https://doi.org/10.3390/atmos15080936, 2024.

Zhang, X. and Xu, M.: Assessing the Effects of Photovoltaic Powerplants on Surface Temperature Using Remote Sensing Techniques, Remote Sens., 12, 1825, https://doi.org/10.3390/rs12111825, 2020.